JACS
JOURNAL OF THE AMERICAN CHEMICAL SOCIETY
pubs.acs.org/JACS
Article

Bridge Sites of Au Surfaces Are Active for Electrocatalytic CO_2 Reduction

Zixu Tao, Adam J. Pearce, James M. Mayer, and Hailiang Wang*

Cite This: J. Am. Chem. Soc. 2022, 144, 8641−8648
Read Online
ACCESS | Metrics & More | Article Recommendations | Supporting Information

ABSTRACT: Prior in situ attenuated total reflectance Fourier transform infrared (ATR−FTIR) studies of electrochemical CO_2 reduction catalyzed by Au, one of the most selective and active electrocatalysts to produce CO from CO_2, suggest that the reaction proceeds solely on the top sites of the Au surface. This finding is worth updating with an improved spectroelectrochemical system where in situ IR measurements can be performed under real reaction conditions that yield high CO selectivity. Herein, we report the preparation of an Au-coated Si ATR crystal electrode with both high catalytic activity for CO_2 reduction and strong surface enhancement of IR signals validated in the same spectroelectrochemical cell, which allows us to probe the adsorption and desorption behavior of bridge-bonded *CO species (*CO_B). We find that the Au surface restructures irreversibly to give an increased number of bridge sites for CO adsorption within the initial tens of seconds of CO_2 reduction. By studying the potential-dependent desorption kinetics of *CO_B and quantifying the steady-state surface concentration of *CO_B under reaction conditions, we further show that *CO_B are active reaction intermediates for CO_2 reduction to CO on this Au electrode. At medium overpotential, as high as 38% of the reaction occurs on the bridge sites.

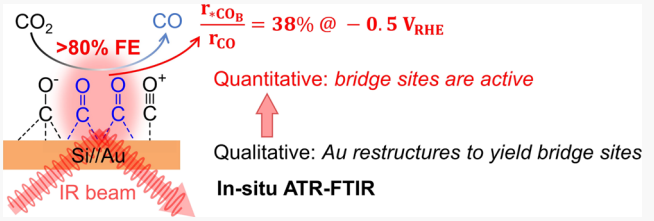

1. INTRODUCTION

Electrocatalytic CO_2 reduction reactions are explored as a viable means to produce carbon-neutral chemicals.[1−7] The rich chemistry of carbon enables CO_2 electroreduction to generate a large variety of products including single-carbon (C_1) and multi-carbon (C_{2+}) species.[8−18] As the simplest two-electron reduction product, CO is perhaps the most accessible species from CO_2 reduction and finds wide application in industrial processes such as the Fischer−Tropsch reaction[19] and hydroformylation.[20] In addition, CO can be electrochemically upgraded to C_{2+} products.[21,22] Different kinds of materials including metals,[23−27] metal coordination compounds/materials,[28−33] and metal-free materials[34−36] have been found to be active for CO_2 electroreduction to CO. Among them, Au metal is arguably the most well-known for its outstanding selectivity and activity. Polycrystalline Au without any modification or special treatment can achieve high Faradaic efficiency (FE) for CO_2-to-CO conversion.[37,38] Catalyst structure optimization and reaction condition engineering can further improve the selectivity and significantly lower the overpotential.[27,39−42]

Interestingly, rough Au surfaces can enhance vibrational absorption via surface plasmon resonance (known as surface enhanced IR absorption spectroscopy, SEIRAS). This enables the application of in situ attenuated total reflectance (ATR) Fourier transform infrared (FTIR) spectroscopy to detect sub-monolayer coverages of adsorbates for mechanistic understanding under reaction-relevant conditions.[43−53] Surendranath et al. were among the first to study Au-catalyzed CO_2 electroreduction with in situ ATR−FTIR, and linearly bonded or atop *CO (*CO_L) and bridge-bonded *CO (*CO_B) were observed at CO_2 reduction potentials.[45] However, the use of a Pt counter electrode led to some controversy.[46,54] Xu and coworkers performed similar measurements in a Pt-free setting and observed only *CO_L species at positive electrode potentials.[46] More recently, Surendranath et al. reported observation of irreversibly bonded *CO_B species in experiments that followed recommended practices to mitigate contamination,[55] which reflects the dependence of Au surface structures/properties on electrode preparation. Other studies of this kind probed reactants, reaction intermediates, and/or electrolyte species on Au surfaces.[41,50−53,55−57] Almost all these studies agree that *CO_L is the only active form of *CO on Au.[45,46,51,52,55,57] However, they share one notable limitation that the catalytic performance, that is, selectivity, activity, and stability, of the Au material deposited on the ATR crystal has never been validated in the spectroelectrochemical cell,[45,46,51,52,55] which makes it difficult to tie spectroscopic observations directly to catalytic reactivity and to exclude interference from side reaction or contamination. While some latest work started to validate catalytic performance of ATR

Received: January 28, 2022
Published: May 4, 2022

Downloaded via YALE UNIV on July 27, 2022 at 20:50:49 (UTC).
See https://pubs.acs.org/sharingguidelines for options on how to legitimately share published articles.

© 2022 American Chemical Society

https://doi.org/10.1021/jacs.2c01098
J. Am. Chem. Soc. 2022, 144, 8641−8648

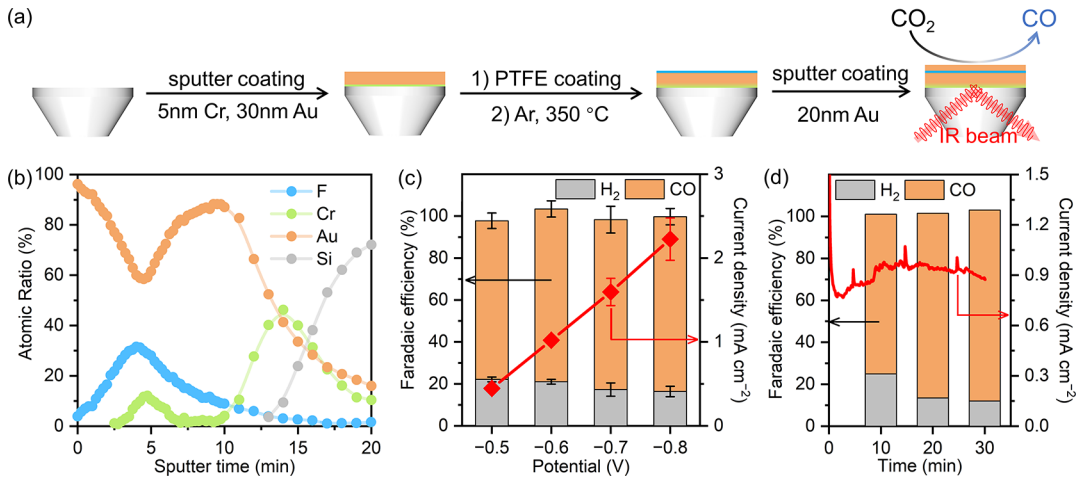

Figure 1. (a) Preparation of the Si//Au electrode. (b) XPS depth profile of Si//Au. (c) CO_2 reduction performance of Si//Au in 0.1 M $KHCO_3$. Error bars represent standard deviations from measurements of three independently prepared electrodes. (d) FE and current density of 30 min CO_2 reduction electrolysis by Si//Au at −0.6 V.

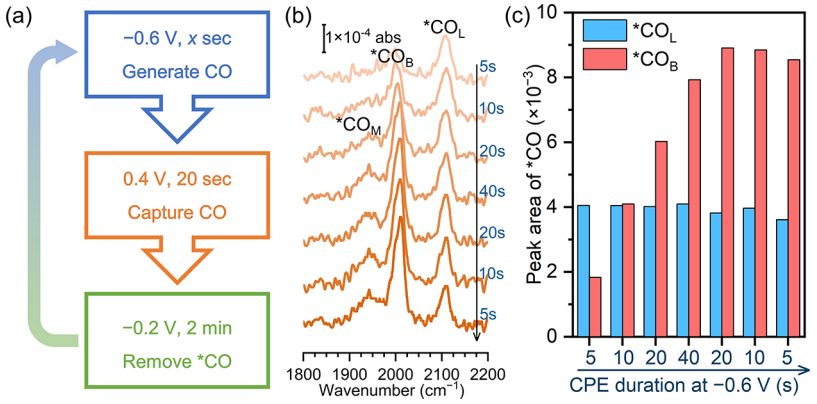

Figure 2. (a) Potential step program for studying CO adsorption on Au. A total of seven cycles are performed in which the time at −0.6 V is varied in the sequence of 5, 10, 20, 40, 20, 10, and 5 s. (b) ATR−FTIR spectra recorded at 0.4 of each potential cycle. Each spectrum is labeled with the time of CO_2 reduction at −0.6 V prior to the 0.4 V step. Each spectrum is averaged from 14 scans. (c) Peak areas of $*CO_L$ and $*CO_B$ observed at 0.4 V.

electrodes,[57] the sensitivity of electrode properties to preparation conditions[47,48,55] entails such validation to be a standard practice. Meanwhile, new electrode structures should be investigated to enrich the prevalent understanding of the reaction mechanism(s).

In this work, we successfully develop a new procedure to deposit a both catalytically and spectroscopically active Au layer on the surface of a Si ATR crystal. The resulting Si//Au electrode, as measured in the spectroelectrochemical cell, exhibits high FEs of 80−90% for CO_2 reduction to CO in the potential range from −0.5 to −0.8 V versus RHE (RHE = reversible hydrogen electrode; all potentials are with respect to RHE unless otherwise stated) together with reasonable current densities and stability. This catalytic performance is on par with that of a typical polycrystalline Au catalytic electrode measured in a standard H-type electrochemical cell, allowing us to carry out an in situ ATR−FTIR study of an Au electrode with benchmarked CO_2 reduction reactivity. We find that the Au surface restructures within the initial tens of seconds of CO_2 reduction to give an increased number of bridge sites for CO adsorption, which has not been reported previously. Using time-resolved scan (TRS), the kinetics of $*CO_B$ desorption from the Au surface is for the first time measured as a function of the applied electrode potential. $*CO_B$ surface concentration is quantified by electrochemical titration and correlated to the IR peak area. On the basis of these results, we derive the contribution of the $*CO_B$ pathway to the total current of CO_2 reduction, which turns out to be a notable portion in the medium overpotential range. This amends the conventional knowledge that $*CO_B$ is a spectator in Au-catalyzed CO_2 electroreduction.

2. RESULTS AND DISCUSSION

Our Si//Au electrode is prepared following the procedure illustrated in Figure 1a (experimental details are provided in the Supporting Information). First, a Cr/Au layer is deposited on the total reflection surface of the Si ATR crystal, followed by a spin-coated thin poly(tetrafluoroethylene) (PTFE) layer. The crystal is then annealed at 350 °C in an Ar atmosphere. The annealed Cr/Au layer renders desirable electrical conductivity, mechanical strength, and adhesion with the Si substrate.[58] PTFE serves as a binder for the Au catalyst layer to be deposited and facilitates delivery of the gas reactant CO_2.[59−61] Finally, another Au layer is deposited to render the electrocatalytic activity for CO_2 reduction (Figure S1a,b). X-ray photoelectron spectroscopy (XPS) depth profiling reveals

https://doi.org/10.1021/jacs.2c01098
J. Am. Chem. Soc. 2022, 144, 8641−8648

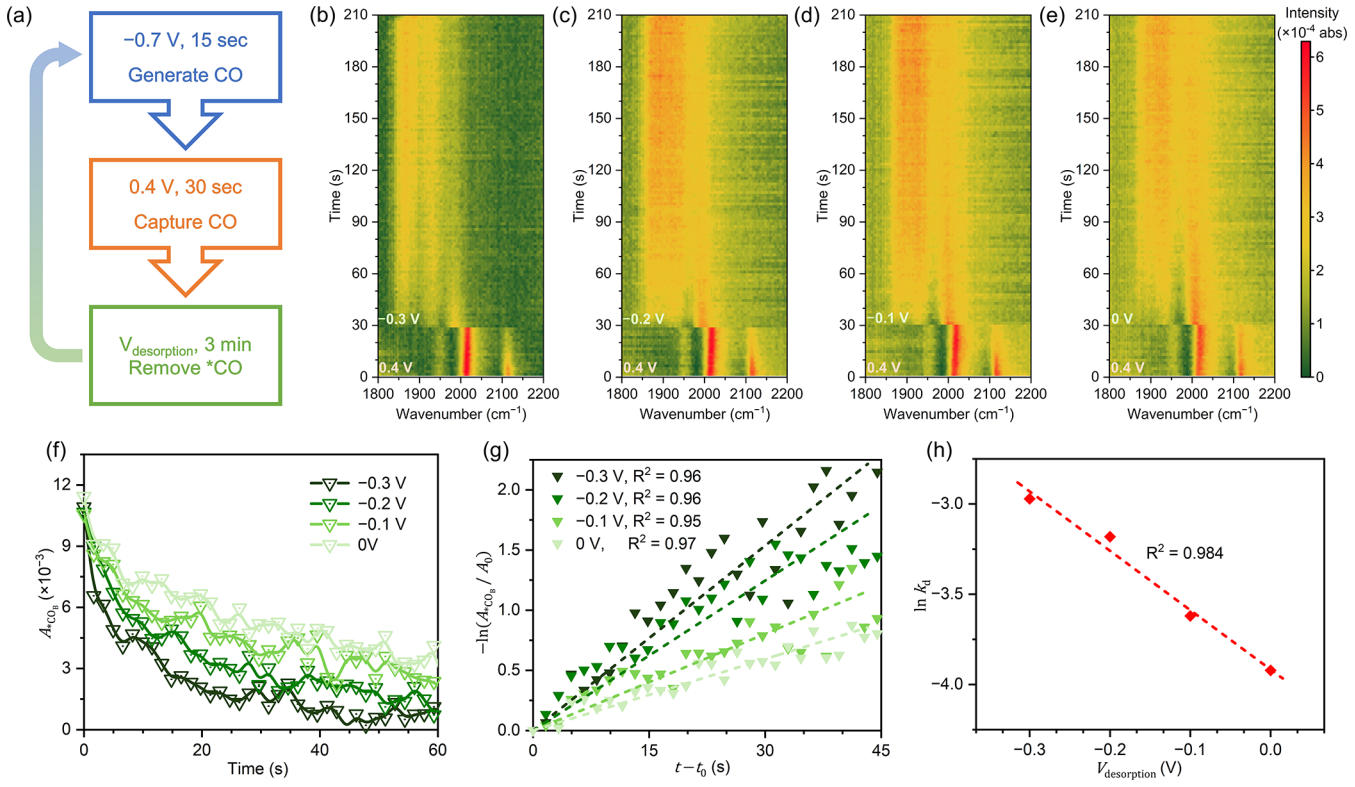

Figure 3. (a) Potential step program for studying the desorption kinetics of $*CO_B$. A total of four cycles are performed in which $V_{desorption}$ is varied in the sequence of −0.3, −0.2, −0.1, and 0 V. (b–e) Heatmaps of TRS ATR–FTIR spectra recorded at 0.4 V and $V_{desorption}$ for each cycle. (f) Desorption profiles of $*CO_B$ at varied $V_{desorption}$. (g) Fitting desorption profiles to first-order kinetics. (h) Potential dependence of the desorption rate constants.

the Si/Cr/Au/PTFE/Au multi-layer structure as expected (Figure 1b). We note that some Cr has diffused through the bottom Au layer after annealing.[58,62] The topmost Au layer manifests a rough surface consisted of 20 nm particles (Figure S2). The Si//Au electrode is assembled into a home-modified ATR–IR spectroelectrochemical cell (Figure S3a,b) and evaluated for its catalytic performance for CO_2 reduction in purified 0.1 M $KHCO_3$ aqueous electrolyte. CO is detected by gas chromatography at −0.5 V, and FE(CO) stays over 80% at more negative potentials (Figure 1c). Both FE(CO) and current density are stable for at least 30 min of continuous operation at −0.6 V (Figure 1d), making it sufficient for ATR–FTIR measurements. This performance is on par with 20 nm Au sputter-coated on a carbon fiber paper electrode (Figure S1c) which is tested in a standard H-cell (Figure S3c,d), representing the typical reactivity of polycrystalline Au electrodes.[38,63]

Successful validation of the catalytic performance of our Si//Au electrode in the spectroelectrochemical cell enables us to perform ATR–FTIR studies of Au under real CO_2 reduction conditions. A potential step program featuring three electrode potentials is adopted (Figure 2a). Constant potential electrolysis (CPE) is first performed at −0.6 V for CO_2 reduction to take place. Then, the potential is changed to 0.4 V for the Au surface to adsorb some of the CO generated earlier and to be probed by IR.[46] After that the potential is adjusted to −0.2 V to allow for CO desorption and regeneration of the Au sites (Figure S4).[46] This sequence is repeated with a varied duration of the −0.6 V step. After the first 5 s of CO_2 reduction at −0.6 V, a band at 2108 cm^{-1} is observed at 0.4 V, which is assigned to $*CO_L$ adsorbed on singlefold top sites (Figure 2b), consistent with previous reports.[45,46,52,55,57] A weaker band centered at around 2000 cm^{-1} is also observed and assigned to be $*CO_B$ adsorbed on twofold bridge sites.[47,64] Note that this vibrational frequency is considerably higher than that of *CO previously reported to be induced by impurities/contamination.[46,54] As the potential step sequence continues with increasingly longer CO_2 reduction, the area of the $*CO_L$ peak remains largely unchanged, whereas the $*CO_B$ peak grows evidently with a slight blue shift of 9 cm^{-1} and becomes the dominant *CO species (Figure 2c). Concomitantly, an additional band with much weaker intensity emerges at around 1940 cm^{-1}, which we assign as CO adsorbed on multifold Au sites ($*CO_M$).[47] Note that both $*CO_B$ and $*CO_M$ have previously been observed on Au surfaces.[47] As the potential step sequence further proceeds with gradually reduced CO_2 reduction durations, both $*CO_B$ and $*CO_L$ bands remain largely unchanged, which suggests that the increased amount of $*CO_B$ is not dependent on the CO_2 reduction duration but is a direct result of some surface restructuring induced by the reaction conditions that forms more bridge sites. When the CO_2 reduction potential in this sequence is changed to −0.7 V, similar enrichment of $*CO_B$ can be observed in a smaller amount of CO_2 reduction time (Figure S5), indicating a larger driving force for restructuring under a more reducing condition. Consistently, no $*CO_B$ can be detected at 0.4 V even after 12 cycles of 5 s CO_2 reduction at −0.5 V (Figure S6). When the sequence starts with a fresh electrode under a N_2 atmosphere and is switched to CO_2 from the second cycle (Figure S7a,d–h), the $*CO_B$ band is stronger than $*CO_L$ almost immediately after the switch and appears to further

https://doi.org/10.1021/jacs.2c01098
J. Am. Chem. Soc. 2022, 144, 8641–8648

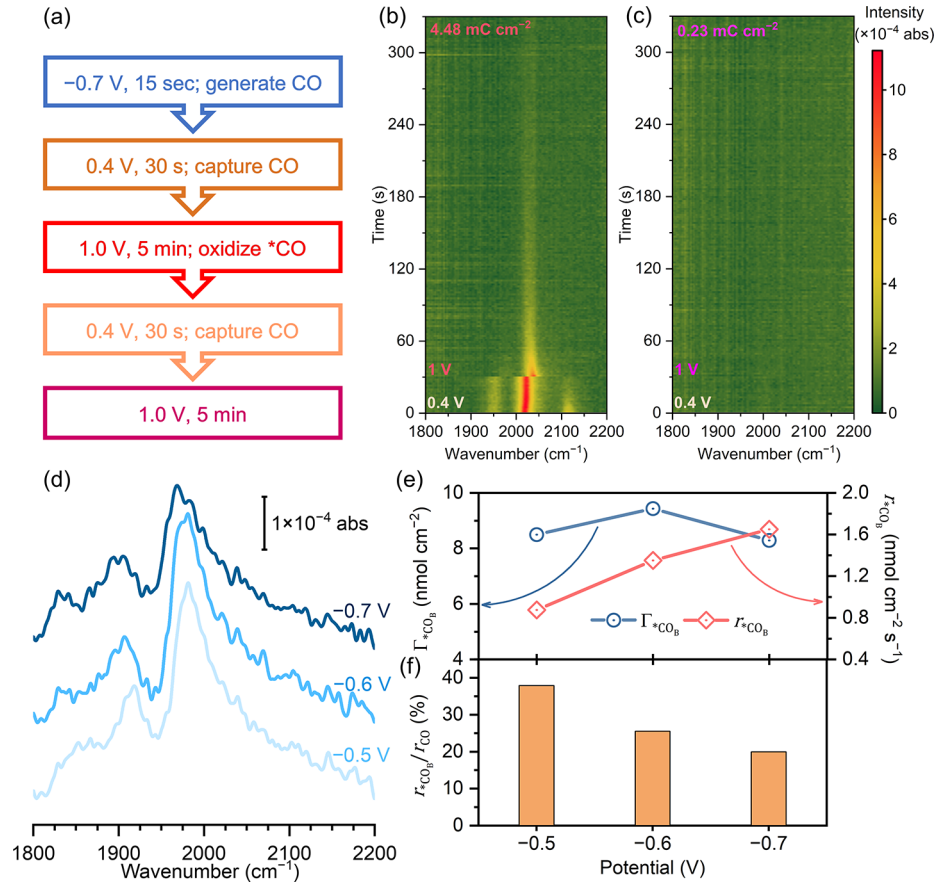

Figure 4. (a) Potential step program for quantifying Γ_{*CO}. After CO is generated at −0.7 V, the electrode potential is cycled twice between 0.4 and 1.0 V. (b–c) Heatmaps of TRS ATR–FTIR spectra recorded at 0.4 and 1.0 V for the first (b) and second (c) potential cycles. Amount of charge recorded at 1.0 V is labeled on each graph. (d) Representative ATR–FTIR spectra recorded at CO_2 reduction potentials. (e) Steady-state Γ_{*CO_B} and $*CO_B$ desorption rate at CO_2 reduction potentials. (f) Potential-dependent share of the $*CO_B$ pathway in total CO production.

grow with longer CO_2 reduction (Figure S7b,c), suggesting that the Au surface restructuring is mainly induced by the electrochemical condition but may be augmented by the presence of CO_2.

The restructuring to expose/activate more bridge sites within the first tens of seconds of electrochemical CO_2 reduction has not been reported before for Au. Because this phenomenon was not observed in previous SEIRAS studies with Au ATR electrodes prepared by the conventional wet method,[45,46,50,55,57] we suspect it may be related to differences in electrode preparation which can influence surface roughness, crystallinity, and nanostructures as well as catalytic performance. While the restructuring of our Au electrodes may not be universal, it provides us a model system to answer the fundamental question whether $*CO_B$ could be an active intermediate of the CO_2 reduction reaction. Considering the relatively weak adsorption strength of $*CO_B$ on our Au electrode indicated by its higher vibrational frequency compared to $*CO_B$ on other noble metals,[27,52,65−70] we hypothesize that $*CO_B$ from CO_2 reduction could desorb to form CO. To test this hypothesis, the desorption kinetics of $*CO_B$ is first measured (Scheme S1). CO is generated from CO_2 reduction at −0.7 V and then captured at 0.4 V, after which the electrode potential is held at $V_{desorption}$ to measure $*CO_B$ desorption using TRS ATR–FTIR with a temporal resolution of 1.648 s (Figure 3a). From the recorded spectra plotted in Figure 3b–e, the desorption of $*CO_B$ is clearly visible at ∼1985 cm^{-1}. Two broad bands centered at 1870 and 1928 cm^{-1} become prominent in the later minutes at $V_{desorption}$, which are possibly $*COOH$[71] and $*CO_M$, respectively. Therefore, the desorption profile of $*CO_B$ at each $V_{desorption}$, that is, IR peak area versus time, is acquired from the initial 60 s at $V_{desorption}$ to ensure correct quantification of $*CO_B$ desorption (Figure 3f). Here, we assume the surface concentration (Γ_{*CO_B}, the number of CO molecules adsorbed on bridge sites normalized to the geometric area of the Si//Au electrode) is proportional to the IR peak area (A_{*CO_B}).[72] The desorption profiles can be simply fitted by the first-order kinetics equation[73]

$$-\ln\frac{\Gamma_{*CO_B}}{\Gamma_0} = -\ln\frac{A_{*CO_B}}{A_0} = k_d(t - t_0) \quad (1)$$

where k_d is the rate constant, and Γ_0 (A_0) refers to $*CO_B$ surface concentration (IR peak area) at t_0 moment. After acquiring the k_d values for four different desorption potentials with reasonable linearity (Figure 3g), we analyze the potential dependence of the desorption rate constant. We find the relationship between k_d and $V_{desorption}$ follows a simple exponential equation (Figure 3h)[74,75]

$$\ln k_d = a \cdot V_{desorption} + b \quad (2)$$

where a and b are both constants. Extrapolating this equation allows us to estimate k_d values at CO_2 reduction potentials

https://doi.org/10.1021/jacs.2c01098
J. Am. Chem. Soc. 2022, 144, 8641−8648

where the generation of CO from CO_2 reduction prevents a direct measurement of the desorption kinetics.

To determine the value of Γ_{*CO_B}, which is needed to calculate the CO production rate via the $*CO_B$ pathway, we quantify Γ_{*CO} at 0.4 V with electrochemical titration and correlate it with the IR peak area (Scheme S1).[43,44] A potential step program is adopted (Figure 4a) and monitored with TRS ATR−FTIR. CO is generated at −0.7 V, captured at 0.4 V, and then electrochemically stripped at 1.0 V (oxidized to CO_2). By holding the potential at 0.4 V for 30 s, unstable reductive intermediates and free CO in the local electrolyte are removed under continuous CO_2 bubbling. The corresponding IR spectra well reflect the capture and oxidative removal of $*CO_L$, $*CO_B$, and $*CO_M$ (Figure 4b). The 0.4 and 1.0 V steps are repeated once to measure the background (e.g., contribution from double layer capacitance), during which no *CO is observed by IR (Figure 4c). Based on the net anodic charge, the total Γ_{*CO} is determined to be 22.0 nmol cm^{-2} (geometric surface area) at the last moment of 0.4 V (corresponding to the IR peak area of 0.0322, Figure S8). We note that this value is substantially higher than the atomic density of the single-crystal Au(111) surface (2.01 nmol cm^{-2}) as a result of the high surface roughness of the deposited Au.[47,48]

Assuming the ratio between the IR peak area and surface concentration of each type of *CO is the same constant regardless of the electrode potential and surface concentration within the IR intensity range of this study, we can then determine Γ_{*CO_B} under CO_2 reduction conditions using this relationship

$$\Gamma_{*CO_B} = \frac{A_{*CO_B}}{0.0322} \cdot 22.0 \text{ nmol cm}^{-2} \quad (3)$$

We are able to acquire steady-state A_{*CO_B} under CO_2 reduction reaction conditions by directly holding the electrode potential at −0.7 and −0.6 V (Figure S9a,b). We note that the accumulation of $*CO_B$ at −0.6 V is considerably slower than that at −0.7 V (Figure S9d,e) likely because of the slower restructuring to generate bridge sites (Figures 2 and S5). At −0.5 V where the restructuring is expected to be even slower, $*CO_B$ is not detected by IR within 5 min (Figure S9c). Therefore, we first perform CO_2 reduction at −0.7 V and then switch the electrode potential stepwise from 0.2 to −0.8 V to measure steady state Γ_{*CO_B} at each CO_2 reduction potential (−0.5 to −0.8 V) using the same Si//Au electrode (Figure S10a). In situ ATR−FTIR reveals gradual *CO desorption and decline of A_{*CO_B} from 0.2 to −0.3 V (Figure S10b,c), agreeing with the previous observation of faster desorption at more negative potential in this region (Figure 3). As the potential becomes more negative, A_{*CO_B} evidently increases due to CO production from CO_2 reduction. The A_{*CO_B} values measured this way for −0.6 and −0.7 V match well with those obtained from directly setting the electrode at CO_2 reduction potentials (Figure S9e). The steady-state IR spectra at −0.5, −0.6, and −0.7 V are shown in Figure 4d and the corresponding Γ_{*CO_B} values are determined using eq 3 (Figure 4e). We then calculate the desorption rate of $*CO_B$, r_{*CO_B}, which is equal to the reaction rate of CO_2 reduction to CO via the $*CO_B$ pathway at steady state (CO re-adsorption at these potentials is unlikely on Au surfaces[46]) using eq 4 (Figure 4e)

$$r_{*CO_B} = \Gamma_{*CO_B} \times k_d \quad (4)$$

The total CO production rate r_{CO} is given by eq 5

$$r_{CO} = j_{CO} \div F \div 2 \quad (5)$$

where j_{CO} is the CO partial current density (Figure 1c) and F is the Faraday constant. Comparing r_{*CO_B} to r_{CO} evidently shows that the $*CO_B$ pathway accounts for a significant proportion of CO_2 reduction to CO (Figure 4f). For example, at −0.5 V, approximately 38% of the reaction occurs on the bridge sites. We note that r_{*CO_B} increases with overpotential (Figure 4e), which is reasonable because of faster $*CO_B$ desorption at more negative potentials (Figure 3). It also appears that the contribution of $*CO_B$ to total CO production decreases at larger overpotential (Figure 4f), which may be related to the competition between $*CO_B$ and $*CO_L$ pathways.

Finally, we note that our aforementioned results are, as best we can tell, free from any significant influence of possible contamination. The spectroelectrochemical cell is configured with an anionic exchange membrane and a high-purity graphite counter electrode, and the electrolyte is purified before use, following a recommended protocol to avoid contamination from metal impurities.[54] The electrochemically purified $KHCO_3$ electrolyte has been used in our lab for years to benchmark many different electrocatalysts for different electrocatalytic CO_2 reduction products with no sign of interference or contamination.[12−18,76−83] To further confirm that our IR results are not caused by contamination from the electrolyte, we show that we can reliably reproduce the spectroelectrochemical results in Figure 2 with an ultrahigh-purity $KHCO_3$ electrolyte (Figure S11, see the Supporting Information for electrolyte preparation and purification details). Our Si//Au electrode manifests selective and stable CO_2 reduction activity characteristic of clean Au surfaces. Consistently, no metal impurities are detected on the surface by XPS either before or after electrocatalysis (Figure S12). More specifically, a control electrode without the topmost 20 nm Au layer has essentially no catalytic activity for CO_2 reduction to CO (Figure S1b), and no CO re-adsorption can be observed in the in situ ATR−FTIR measurement (Figure S13). This result adds additional support to the conclusion that the use of the Cr adhesion layer (or any contamination from it) is not responsible for the catalytic and spectroscopic features that we observe on the Si//Au electrode. In addition, the above-mentioned lack of $*CO_B$ re-adsorption at 0.4 V (only $*CO_L$ is observed) while we limit the prior CO_2 reduction potential to −0.5 V (Figure S6) is another piece of evidence against possible contamination in our system.

3. CONCLUSIONS

In summary, we have presented a time-resolved in situ ATR−FTIR study of Au-catalyzed electrochemical CO_2 reduction. From quantitatively probing bridge-bonded *CO species across a wide electrode potential range including the CO_2 reduction region, we have for the first time revealed that the Au surface can restructure during the initial phase of CO_2 reduction, and that the resulting bridge sites are catalytically active for CO production. Future studies employing advanced characterization techniques that are currently under rapid development, for example, high-resolution scanning probe microscopy imaging under electrochemical conditions, could help visualize the atomic-scale restructuring.

https://doi.org/10.1021/jacs.2c01098
J. Am. Chem. Soc. 2022, 144, 8641−8648

■ ASSOCIATED CONTENT

Supporting Information

The Supporting Information is available free of charge at https://pubs.acs.org/doi/10.1021/jacs.2c01098.

Experimental details, electrocatalytic performance, SEM image of Si//Au surface, structures and photographs of the spectroelectrochemical and H-type cells, XPS spectra, and additional ATR−FTIR results (PDF)

■ AUTHOR INFORMATION

Corresponding Author

Hailiang Wang − *Department of Chemistry, Yale University, New Haven, Connecticut 06520, United States; Energy Sciences Institute, Yale University, West Haven, Connecticut 06516, United States;* orcid.org/0000-0003-4409-2034; Email: hailiang.wang@yale.edu

Authors

Zixu Tao − *Department of Chemistry, Yale University, New Haven, Connecticut 06520, United States; Energy Sciences Institute, Yale University, West Haven, Connecticut 06516, United States;* orcid.org/0000-0002-6670-1796

Adam J. Pearce − *Department of Chemistry, Yale University, New Haven, Connecticut 06520, United States*

James M. Mayer − *Department of Chemistry, Yale University, New Haven, Connecticut 06520, United States;* orcid.org/0000-0002-3943-5250

Complete contact information is available at: https://pubs.acs.org/10.1021/jacs.2c01098

Notes

The authors declare no competing financial interest.

■ ACKNOWLEDGMENTS

This work was supported by the US National Science Foundation (grant CBET2028351) to H.W. Z.T. acknowledges a Dox Fellowship from Yale University. The Bruker VERTEX instrument was purchased and modified in-house primarily with funds from National Institutes of Health (NIH) Instrument Supplement to grant 2R01GM050422, with components purchased with funds from the Air Force Office of Scientific Research under award no. FA9550-18-1-0420 to a Multidisciplinary Research Program of the University Research Initiative (MURI) "Molecular-Scale Studies of Liquid−Solid Interfaces in Electrochemical Processes" and from the Center for Molecular Electrocatalysis (CME), an Energy Frontier Research Center funded by the U.S. Department of Energy, Office of Science, Office of Basic Energy Sciences. The VeeMAX III ATR accessory used in the current work was later purchased using funds from the Center for Hybrid Approaches to Solar Energy for liquid fuels (CHASE), an Energy Innovation Hub funded by the U.S. Department of Energy, Office of Science, Office of Basic Energy Sciences under award number DE-SC0021173. A.J.P.'s development of the IR instrument was supported by a postdoctoral fellowship from the National Institutes of Health (NIH), award no. 1F32GM140723-01A1. J.M.M.'s work on noble metal electrochemical interfaces was supported by the Air Force Office of Scientific Research under the MURI award listed above.

■ REFERENCES

(1) Thonemann, N.; Pizzol, M. Consequential life cycle assessment of carbon capture and utilization technologies within the chemical industry. *Energy Environ. Sci.* **2019**, *12*, 2253−2263.

(2) Ross, M. B.; De Luna, P.; Li, Y.; Dinh, C.-T.; Kim, D.; Yang, P.; Sargent, E. H. Designing materials for electrochemical carbon dioxide recycling. *Nat. Catal.* **2019**, *2*, 648−658.

(3) Liu, Z.; Wang, K.; Chen, Y.; Tan, T.; Nielsen, J. Third-generation biorefineries as the means to produce fuels and chemicals from CO_2. *Nat. Catal.* **2020**, *3*, 274−288.

(4) Gao, W.; Liang, S.; Wang, R.; Jiang, Q.; Zhang, Y.; Zheng, Q.; Xie, B.; Toe, C. Y.; Zhu, X.; Wang, J.; Huang, L.; Gao, Y.; Wang, Z.; Jo, C.; Wang, Q.; Wang, L.; Liu, Y.; Louis, B.; Scott, J.; Roger, A.-C.; Amal, R.; He, H.; Park, S.-E. Industrial carbon dioxide capture and utilization: state of the art and future challenges. *Chem. Soc. Rev.* **2020**, *49*, 8584−8686.

(5) Sakakura, T.; Choi, J.-C.; Yasuda, H. Transformation of Carbon Dioxide. *Chem. Rev.* **2007**, *107*, 2365−2387.

(6) Tang, C.; Zheng, Y.; Jaroniec, M.; Qiao, S. Z. Electrocatalytic Refinery for Sustainable Production of Fuels and Chemicals. *Angew. Chem., Int. Ed.* **2021**, *60*, 19572.

(7) Artz, J.; Müller, T. E.; Thenert, K.; Kleinekorte, J.; Meys, R.; Sternberg, A.; Bardow, A.; Leitner, W. Sustainable Conversion of Carbon Dioxide: An Integrated Review of Catalysis and Life Cycle Assessment. *Chem. Rev.* **2018**, *118*, 434−504.

(8) Wagner, A.; Sahm, C. D.; Reisner, E. Towards molecular understanding of local chemical environment effects in electro- and photocatalytic CO_2 reduction. *Nat. Catal.* **2020**, *3*, 775−786.

(9) Ding, P.; Zhao, H.; Li, T.; Luo, Y.; Fan, G.; Chen, G.; Gao, S.; Shi, X.; Lu, S.; Sun, X. Metal-based electrocatalytic conversion of CO_2 to formic acid/formate. *J. Mater. Chem. A* **2020**, *8*, 21947−21960.

(10) Wu, Y.; Cao, S.; Hou, J.; Li, Z.; Zhang, B.; Zhai, P.; Zhang, Y.; Sun, L. Rational Design of Nanocatalysts with Nonmetal Species Modification for Electrochemical CO_2 Reduction. *Adv. Energy Mater.* **2020**, *10*, 2000588.

(11) Lee, C. W.; Yang, K. D.; Nam, D.-H.; Jang, J. H.; Cho, N. H.; Im, S. W.; Nam, K. T. Defining a Materials Database for the Design of Copper Binary Alloy Catalysts for Electrochemical CO_2 Conversion. *Adv. Mater.* **2018**, *30*, 1704717.

(12) Tao, Z.; Wu, Z.; Wu, Y.; Wang, H. Activating Copper for Electrocatalytic CO_2 Reduction to Formate via Molecular Interactions. *ACS Catal.* **2020**, *10*, 9271−9275.

(13) Wu, Y.; Jiang, Z.; Lu, X.; Liang, Y.; Wang, H. Domino electroreduction of CO_2 to methanol on a molecular catalyst. *Nature* **2019**, *575*, 639−642.

(14) Tao, Z.; Wu, Z.; Yuan, X.; Wu, Y.; Wang, H. Copper Gold Interactions Enhancing Formate Production from Electrochemical CO_2 Reduction. *ACS Catal.* **2019**, *9*, 10894−10898.

(15) Cai, Z.; Wu, Y.; Wu, Z.; Yin, L.; Weng, Z.; Zhong, Y.; Xu, W.; Sun, X.; Wang, H. Unlocking Bifunctional Electrocatalytic Activity for CO_2 Reduction Reaction by Win-Win Metal−Oxide Cooperation. *ACS Energy Lett.* **2018**, *3*, 2816−2822.

(16) Wu, Y.; Jiang, J.; Weng, Z.; Wang, M.; Broere, D. L. J.; Zhong, Y.; Brudvig, G. W.; Feng, Z.; Wang, H. Electroreduction of CO_2 Catalyzed by a Heterogenized Zn-Porphyrin Complex with a Redox-Innocent Metal Center. *ACS Cent. Sci.* **2017**, *3*, 847−852.

(17) Weng, Z.; Zhang, X.; Wu, Y.; Huo, S.; Jiang, J.; Liu, W.; He, G.; Liang, Y.; Wang, H. Self-Cleaning Catalyst Electrodes for Stabilized CO_2 Reduction to Hydrocarbons. *Angew. Chem., Int. Ed.* **2017**, *56*, 13135.

(18) Huo, S.; Weng, Z.; Wu, Z.; Zhong, Y.; Wu, Y.; Fang, J.; Wang, H. Coupled Metal/Oxide Catalysts with Tunable Product Selectivity for Electrocatalytic CO_2 Reduction. *ACS Appl. Mater. Interfaces* **2017**, *9*, 28519−28526.

(19) Martinelli, M.; Gnanamani, M. K.; LeViness, S.; Jacobs, G.; Shafer, W. D. An overview of Fischer-Tropsch Synthesis: XtL processes, catalysts and reactors. *Appl. Catal., A* **2020**, *608*, 117740.

(20) Ojima, I.; Tsai, C.-Y.; Tzamarioudaki, M.; Bonafoux, D. *Organic Reactions*; Denmark, S. E., Ed.; John Wiley & Sons, Inc., 2004; pp 2−10.
(21) Li, C. W.; Ciston, J.; Kanan, M. W. Electroreduction of carbon monoxide to liquid fuel on oxide-derived nanocrystalline copper. *Nature* **2014**, *508*, 504−507.
(22) Luc, W.; Fu, X.; Shi, J.; Lv, J.-J.; Jouny, M.; Ko, B. H.; Xu, Y.; Tu, Q.; Hu, X.; Wu, J.; Yue, Q.; Liu, Y.; Jiao, F.; Kang, Y. Two-dimensional copper nanosheets for electrochemical reduction of carbon monoxide to acetate. *Nat. Catal.* **2019**, *2*, 423−430.
(23) Abeyweera, S. C.; Yu, J.; Perdew, J. P.; Yan, Q.; Sun, Y. Hierarchically 3D Porous Ag Nanostructures Derived from Silver Benzenethiolate Nanoboxes: Enabling CO_2 Reduction with a Near-Unity Selectivity and Mass-Specific Current Density over 500 A/g. *Nano Lett.* **2020**, *20*, 2806−2811.
(24) Raciti, D.; Livi, K. J.; Wang, C. Highly Dense Cu Nanowires for Low-Overpotential CO_2 Reduction. *Nano Lett.* **2015**, *15*, 6829−6835.
(25) Kim, D.; Resasco, J.; Yu, Y.; Asiri, A. M.; Yang, P. Synergistic geometric and electronic effects for electrochemical reduction of carbon dioxide using gold−copper bimetallic nanoparticles. *Nat. Commun.* **2014**, *5*, 4948.
(26) Jansonius, R. P.; Reid, L. M.; Virca, C. N.; Berlinguette, C. P. Strain Engineering Electrocatalysts for Selective CO_2 Reduction. *ACS Energy Lett.* **2019**, *4*, 980−986.
(27) Yuan, X.; Zhang, L.; Li, L.; Dong, H.; Chen, S.; Zhu, W.; Hu, C.; Deng, W.; Zhao, Z.-J.; Gong, J. Ultrathin Pd-Au Shells with Controllable Alloying Degree on Pd Nanocubes toward Carbon Dioxide Reduction. *J. Am. Chem. Soc.* **2019**, *141*, 4791−4794.
(28) Loipersberger, M.; Cabral, D. G. A.; Chu, D. B. K.; Head-Gordon, M. Mechanistic Insights into Co and Fe Quaterpyridine-Based CO_2 Reduction Catalysts: Metal-Ligand Orbital Interaction as the Key Driving Force for Distinct Pathways. *J. Am. Chem. Soc.* **2021**, *143*, 744−763.
(29) Sun, M.-J.; Gong, Z.-W.; Yi, J.-D.; Zhang, T.; Chen, X.; Cao, R. A highly efficient diatomic nickel electrocatalyst for CO_2 reduction. *Chem. Commun.* **2020**, *56*, 8798−8801.
(30) Wang, T.; Sang, X.; Zheng, W.; Yang, B.; Yao, S.; Lei, C.; Li, Z.; He, Q.; Lu, J.; Lei, L.; Dai, L.; Hou, Y. Gas Diffusion Strategy for Inserting Atomic Iron Sites into Graphitized Carbon Supports for Unusually High-Efficient CO_2 Electroreduction and High-Performance Zn-CO_2 Batteries. *Adv. Mater.* **2020**, *32*, 2002430.
(31) Suntrup, L.; Stein, F.; Klein, J.; Wilting, A.; Parlane, F. G. L.; Brown, C. M.; Fiedler, J.; Berlinguette, C. P.; Siewert, I.; Sarkar, B. Rhenium Complexes of Pyridyl-Mesoionic Carbenes: Photochemical Properties and Electrocatalytic CO_2 Reduction. *Inorg. Chem.* **2020**, *59*, 4215−4227.
(32) Zee, D. Z.; Nippe, M.; King, A. E.; Chang, C. J.; Long, J. R. Tuning Second Coordination Sphere Interactions in Polypyridyl−Iron Complexes to Achieve Selective Electrocatalytic Reduction of Carbon Dioxide to Carbon Monoxide. *Inorg. Chem.* **2020**, *59*, 5206−5217.
(33) Li, X.; Bi, W.; Chen, M.; Sun, Y.; Ju, H.; Yan, W.; Zhu, J.; Wu, X.; Chu, W.; Wu, C.; Xie, Y. Exclusive Ni-N_4 Sites Realize Near-Unity CO Selectivity for Electrochemical CO_2 Reduction. *J. Am. Chem. Soc.* **2017**, *139*, 14889−14892.
(34) Chen, C.; Sun, X.; Yan, X.; Wu, Y.; Liu, H.; Zhu, Q.; Bediako, B. B. A.; Han, B. Boosting CO_2 Electroreduction on N,P-Co-doped Carbon Aerogels. *Angew. Chem., Int. Ed.* **2020**, *59*, 11123.
(35) Ni, W.; Xue, Y.; Zang, X.; Li, C.; Wang, H.; Yang, Z.; Yan, Y.-M. Fluorine Doped Cagelike Carbon Electrocatalyst: An Insight into the Structure-Enhanced CO Selectivity for CO_2 Reduction at High Overpotential. *ACS Nano* **2020**, *14*, 2014−2023.
(36) Duan, X.; Xu, J.; Wei, Z.; Ma, J.; Guo, S.; Wang, S.; Liu, H.; Dou, S. Metal-Free Carbon Materials for CO_2 Electrochemical Reduction. *Adv. Mater.* **2017**, *29*, 1701784.
(37) Chen, C.; Zhang, B.; Zhong, J.; Cheng, Z. Selective electrochemical CO_2 reduction over highly porous gold films. *J. Mater. Chem. A* **2017**, *5*, 21955−21964.
(38) Zhu, W.; Michalsky, R.; Metin, Ö.; Lv, H.; Guo, S.; Wright, C. J.; Sun, X.; Peterson, A. A.; Sun, S. Monodisperse Au Nanoparticles for Selective Electrocatalytic Reduction of CO_2 to CO. *J. Am. Chem. Soc.* **2013**, *135*, 16833−16836.
(39) Verma, S.; Hamasaki, Y.; Kim, C.; Huang, W.; Lu, S.; Jhong, H.-R. M.; Gewirth, A. A.; Fujigaya, T.; Nakashima, N.; Kenis, P. J. A. Insights into the Low Overpotential Electroreduction of CO_2 to CO on a Supported Gold Catalyst in an Alkaline Flow Electrolyzer. *ACS Energy Lett.* **2018**, *3*, 193−198.
(40) Zhu, W.; Zhang, Y.-J.; Zhang, H.; Lv, H.; Li, Q.; Michalsky, R.; Peterson, A. A.; Sun, S. Active and Selective Conversion of CO_2 to CO on Ultrathin Au Nanowires. *J. Am. Chem. Soc.* **2014**, *136*, 16132−16135.
(41) Dong, H.; Zhang, L.; Li, L.; Deng, W.; Hu, C.; Zhao, Z. J.; Gong, J. Abundant Ce^{3+} Ions in Au-CeO_x Nanosheets to Enhance CO_2 Electroreduction Performance. *Small* **2019**, *15*, 1900289.
(42) Valenti, M.; Prasad, N. P.; Kas, R.; Bohra, D.; Ma, M.; Balasubramanian, V.; Chu, L.; Gimenez, S.; Bisquert, J.; Dam, B.; Smith, W. A. Suppressing H_2 Evolution and Promoting Selective CO_2 Electroreduction to CO at Low Overpotentials by Alloying Au with Pd. *ACS Catal.* **2019**, *9*, 3527−3536.
(43) Kunimatsu, K.; Aramata, A.; Nakajima, N.; Kita, H. Infrared spectra of carbon monoxide adsorbed on a smooth gold electrode: Part II. Emirs and polarization-modulated irras stuidy of the adsorbed co layer in acidic and alkaline solutions. *J. Electroanal. Chem. Interfacial Electrochem.* **1986**, *207*, 293−307.
(44) Nakajima, H.; Kita, H.; Kunimatsu, K.; Aramata, A. Infrared spectra of carbon monoxide adsorbed on a smooth gold electrode Part I. EMIRS spectra in acid and alkaline solutions. *J. Electroanal. Chem. Interfacial Electrochem.* **1986**, *201*, 175−186.
(45) Wuttig, A.; Yaguchi, M.; Motobayashi, K.; Osawa, M.; Surendranath, Y. Inhibited proton transfer enhances Au-catalyzed CO_2-to-fuels selectivity. *Proc. Natl. Acad. Sci. U.S.A.* **2016**, *113*, E4585−E4593.
(46) Dunwell, M.; Lu, Q.; Heyes, J. M.; Rosen, J.; Chen, J. G.; Yan, Y.; Jiao, F.; Xu, B. The Central Role of Bicarbonate in the Electrochemical Reduction of Carbon Dioxide on Gold. *J. Am. Chem. Soc.* **2017**, *139*, 3774−3783.
(47) Sun, S.-G.; Cai, W.-B.; Wan, L.-J.; Osawa, M. Infrared Absorption Enhancement for CO Adsorbed on Au Films in Perchloric Acid Solutions and Effects of Surface Structure Studied by Cyclic Voltammetry, Scanning Tunneling Microscopy, and Surface-Enhanced IR Spectroscopy. *J. Phys. Chem. B* **1999**, *103*, 2460−2466.
(48) Miyake, H.; Ye, S.; Osawa, M. Electroless deposition of gold thin films on silicon for surface-enhanced infrared spectroelectrochemistry. *Electrochem. Commun.* **2002**, *4*, 973−977.
(49) Kraack, J. P.; Kaech, A.; Hamm, P. Surface Enhancement in Ultrafast 2D ATR IR Spectroscopy at the Metal-Liquid Interface. *J. Phys. Chem. C* **2016**, *120*, 3350−3359.
(50) Dunwell, M.; Yang, X.; Setzler, B. P.; Anibal, J.; Yan, Y.; Xu, B. Examination of Near-Electrode Concentration Gradients and Kinetic Impacts on the Electrochemical Reduction of CO_2 using Surface-Enhanced Infrared Spectroscopy. *ACS Catal.* **2018**, *8*, 3999−4008.
(51) Papasizza, M.; Cuesta, A. In Situ Monitoring Using ATR-SEIRAS of the Electrocatalytic Reduction of CO_2 on Au in an Ionic Liquid/Water Mixture. *ACS Catal.* **2018**, *8*, 6345−6352.
(52) Katayama, Y.; Nattino, F.; Giordano, L.; Hwang, J.; Rao, R. R.; Andreussi, O.; Marzari, N.; Shao-Horn, Y. An *In Situ* Surface-Enhanced Infrared Absorption Spectroscopy Study of Electrochemical CO_2 Reduction: Selectivity Dependence on Surface C-Bound and O-Bound Reaction Intermediates. *J. Phys. Chem. C* **2019**, *123*, 5951−5963.
(53) Wagner, A.; Ly, K. H.; Heidary, N.; Szabó, I.; Földes, T.; Assaf, K. I.; Barrow, S. J.; Sokołowski, K.; Al-Hada, M.; Kornienko, N.; Kuehnel, M. F.; Rosta, E.; Zebger, I.; Nau, W. M.; Scherman, O. A.; Reisner, E. Host-Guest Chemistry Meets Electrocatalysis: Cucurbit[6]uril on a Au Surface as a Hybrid System in CO_2 Reduction. *ACS Catal.* **2020**, *10*, 751−761.

https://doi.org/10.1021/jacs.2c01098
J. Am. Chem. Soc. 2022, 144, 8641−8648

(54) Dunwell, M.; Yang, X.; Yan, Y.; Xu, B. Potential Routes and Mitigation Strategies for Contamination in Interfacial Specific Infrared Spectroelectrochemical Studies. *J. Phys. Chem. C* **2018**, *122*, 24658−24664.
(55) Wuttig, A.; Ryu, J.; Surendranath, Y. Electrolyte Competition Controls Surface Binding of CO Intermediates to CO_2 Reduction Catalysts. *J. Phys. Chem. C* **2021**, *125*, 17042−17050.
(56) Yu, D.; Gao, L.; Sun, T.; Guo, J.; Yuan, Y.; Zhang, J.; Li, M.; Li, X.; Liu, M.; Ma, C.; Liu, Q.; Pan, A.; Yang, J.; Huang, H. Strain-Stabilized Metastable Face-Centered Tetragonal Gold Overlayer for Efficient CO_2 Electroreduction. *Nano Lett.* **2021**, *21*, 1003−1010.
(57) Deng, W.; Yuan, T.; Chen, S.; Li, H.; Hu, C.; Dong, H.; Wu, B.; Wang, T.; Li, J.; Ozin, G. A.; Gong, J. Effect of bicarbonate on CO_2 electroreduction over cathode catalysts. *Fundam. Res.* **2021**, *1*, 432−438.
(58) Todeschini, M.; Bastos da Silva Fanta, A.; Jensen, F.; Wagner, J. B.; Han, A. Influence of Ti and Cr Adhesion Layers on Ultrathin Au Films. *ACS Appl. Mater. Interfaces* **2017**, *9*, 37374−37385.
(59) Lu, Z.; Xu, W.; Ma, J.; Li, Y.; Sun, X.; Jiang, L. Superaerophilic Carbon-Nanotube-Array Electrode for High-Performance Oxygen Reduction Reaction. *Adv. Mater.* **2016**, *28*, 7155−7161.
(60) Xia, C.; Back, S.; Ringe, S.; Jiang, K.; Chen, F.; Sun, X.; Siahrostami, S.; Chan, K.; Wang, H. Confined local oxygen gas promotes electrochemical water oxidation to hydrogen peroxide. *Nat. Catal.* **2020**, *3*, 125−134.
(61) Nguyen, T. N.; Dinh, C.-T. Gas diffusion electrode design for electrochemical carbon dioxide reduction. *Chem. Soc. Rev.* **2020**, *49*, 7488−7504.
(62) Huang, Y.; Qiu, H.; Wang, F.; Pan, L.; Tian, Y.; Wu, P. Effect of annealing on the characteristics of Au/Cr bilayer films grown on glass. *Vacuum* **2003**, *71*, 523−528.
(63) Mezzavilla, S.; Horch, S.; Stephens, I. E. L.; Seger, B.; Chorkendorff, I. Structure Sensitivity in the Electrocatalytic Reduction of CO_2 with Gold Catalysts. *Angew. Chem., Int. Ed.* **2019**, *58*, 3774.
(64) Schumacher, B.; Denkwitz, Y.; Plzak, V.; Kinne, M.; Behm, R. J. Kinetics, mechanism, and the influence of H_2 on the CO oxidation reaction on a Au/TiO_2 catalyst. *J. Catal.* **2004**, *224*, 449−462.
(65) Miyake, H.; Okada, T.; Samjeské, G.; Osawa, M. Formic Acid Electrooxidation on Pd in Acidic Solutions Studied by Surface-Enhanced Infrared Absorption Spectroscopy. *Phys. Chem. Chem. Phys.* **2008**, *10*, 3662−3669.
(66) Gao, D.; Zhou, H.; Cai, F.; Wang, D.; Hu, Y.; Jiang, B.; Cai, W.-B.; Chen, X.; Si, R.; Yang, F.; Miao, S.; Wang, J.; Wang, G.; Bao, X. Switchable CO_2 electroreduction via engineering active phases of Pd nanoparticles. *Nano Res.* **2017**, *10*, 2181−2191.
(67) Qin, X.; Li, H.; Xie, S.; Li, K.; Jiang, T.; Ma, X.-Y.; Jiang, K.; Zhang, Q.; Terasaki, O.; Wu, Z.; Cai, W.-B. Mechanistic Analysis-Guided Pd-Based Catalysts for Efficient Hydrogen Production from Formic Acid Dehydrogenation. *ACS Catal.* **2020**, *10*, 3921−3932.
(68) Jiang, T.-W.; Zhou, Y.-W.; Ma, X.-Y.; Qin, X.; Li, H.; Ding, C.; Jiang, B.; Jiang, K.; Cai, W.-B. Spectrometric Study of Electrochemical CO_2 Reduction on Pd and Pd-B Electrodes. *ACS Catal.* **2021**, *11*, 840−848.
(69) Chang, S. C.; Weaver, M. J. Coverage-dependent dipole coupling for carbon monoxide adsorbed at ordered platinum(111)-aqueous interfaces: Structural and electrochemical implications. *J. Chem. Phys.* **1990**, *92*, 4582−4594.
(70) Yan; Li, Q.-X.; Huo, S.-J.; Ma, M.; Cai, W.-B.; Osawa, M. Ubiquitous Strategy for Probing ATR Surface-Enhanced Infrared Absorption at Platinum Group Metal−Electrolyte Interfaces. *J. Phys. Chem. B* **2005**, *109*, 7900−7906.
(71) Dunwell, M.; Yan, Y.; Xu, B. In Situ Infrared Spectroscopic Investigations of Pyridine-Mediated CO_2 Reduction on Pt Electrocatalysts. *ACS Catal.* **2017**, *7*, 5410−5419.
(72) Vilmin, F.; Bazin, P.; Thibault-Starzyk, F.; Travert, A. Speciation of adsorbates on surface of solids by infrared spectroscopy and chemometrics. *Anal. Chim. Acta* **2015**, *891*, 79−89.
(73) Yamada, T.; Onishi, T.; Tamaru, K. Adsorption-desorption kinetics of carbon monoxide on palladium polycrystalline surfaces. *Surf. Sci.* **1983**, *133*, 533−546.
(74) Redhead, P. A. Thermal desorption of gases. *Vacuum* **1962**, *12*, 203−211.
(75) Noren, D. A.; Hoffman, M. A. Clarifying the Butler−Volmer equation and related approximations for calculating activation losses in solid oxide fuel cell models. *J. Power Sources* **2005**, *152*, 175−181.
(76) Wu, Y.; Yuan, X.; Tao, Z.; Wang, H. Bifunctional electrocatalysis for CO_2 reduction *via* surface capping-dependent metal−oxide interactions. *Chem. Commun.* **2019**, *55*, 8864−8867.
(77) Tao, Z.; Rooney, C. L.; Liang, Y.; Wang, H. Accessing Organonitrogen Compounds via C−N Coupling in Electrocatalytic CO_2 Reduction. *J. Am. Chem. Soc.* **2021**, *143*, 19630−19642.
(78) Tao, Z.; Wu, Y.; Wu, Z.; Shang, B.; Rooney, C.; Wang, H. Cascade electrocatalytic reduction of carbon dioxide and nitrate to ethylamine. *J. Energy Chem.* **2022**, *65*, 367−370.
(79) Wu, Y.; Jiang, Z.; Lin, Z.; Liang, Y.; Wang, H. Direct electrosynthesis of methylamine from carbon dioxide and nitrate. *Nat. Sustain.* **2021**, *4*, 725−730.
(80) Wu, Z.; Huang, L.; Liu, H.; Wang, H. Element-Specific Restructuring of Anion- and Cation-Substituted Cobalt Phosphide Nanoparticles under Electrochemical Water-Splitting Conditions. *ACS Catal.* **2019**, *9*, 2956−2961.
(81) Lu, X.; Wu, Y.; Yuan, X.; Wang, H. An Integrated CO_2 Electrolyzer and Formate Fuel Cell Enabled by a Reversibly Restructuring Pb-Pd Bimetallic Catalyst. *Angew. Chem., Int. Ed.* **2019**, *58*, 4031.
(82) Weng, Z.; Jiang, J.; Wu, Y.; Wu, Z.; Guo, X.; Materna, K. L.; Liu, W.; Batista, V. S.; Brudvig, G. W.; Wang, H. Electrochemical CO_2 Reduction to Hydrocarbons on a Heterogeneous Molecular Cu Catalyst in Aqueous Solution. *J. Am. Chem. Soc.* **2016**, *138*, 8076−8079.
(83) Weng, Z.; Wu, Y.; Wang, M.; Jiang, J.; Yang, K.; Huo, S.; Wang, X.-F.; Ma, Q.; Brudvig, G. W.; Batista, V. S.; Liang, Y.; Feng, Z.; Wang, H. Active sites of copper-complex catalytic materials for electrochemical carbon dioxide reduction. *Nat. Commun.* **2018**, *9*, 415.

https://doi.org/10.1021/jacs.2c01098
J. Am. Chem. Soc. 2022, 144, 8641−8648